第 39 卷 第 3 期 新 型 炭 材 料 （中英文） Vol. 39 No. 3
2024 年 6 月 NEW CARBON MATERIALS Jun. 2024
Cite this : New Carbon Materials, 2024, 39(3): 439-458 **DOI:** 10.1016/S1872-5805(24)60853-X

Advances in graphene/molybdenum dichalcogenide-based van der Waals heterostructure photodetectors

ZHANG Xin-hua[1,†], LIU Wei-di[2,†], GONG You-pin[3,*], LIU Qing-feng[1,*], CHEN Zhi-gang[2,*]

（1. *State Key Laboratory of Materials-Oriented Chemical Engineering*, *College of Chemical Engineering*, *Nanjing Tech University*, *Nanjing* 211816, *China*;
2. *School of Chemistry and Physics*, *ARC Research Hub in Zero-emission Power Generation for Carbon Neutrality*, *and Center for Materials Science*, *Queensland University of Technology*, *Brisbane*, *QLD* 4000, *Australia*;
3. *Center of Quantum Materials and Devices at Institute of Advanced Interdisciplinary Studies*, *College of Physics*, *Chongqing University*, *Chongqing* 400044, *China*）

Abstract: Graphene is widely used in photodetection because of its high carrier mobility and wide spectral absorption range. However, its high dark current caused by its low light absorption severely limits its performance. Molybdenum dihalide (MoX_2, X= S, Se and Te) has a high absorption coefficient, which can compensate for the high dark current in graphene-based photodetectors and result in outstanding photoelectronic properties of those based on a graphene/MoX_2 van der Waals heterostructure (vdWH). In this review, we firstly review working principles, performance indicators, and structures of photodetectors. After that, the significance of graphene/MoX_2 vdWH photodetectors is highlighted from the fundamental perspective. Preparation methodologies and performance enhancement strategies of graphene/MoX_2 vdWH photodetectors are correspondingly summarized. In the end, we highlight the current challenges and future directions of the graphene/MoX_2 vdWH photodetectors. This review will guide the design of high-performance vdWH photodetectors.

Key words: Graphene; Molybdenum dihalide; Heterostructure; Photodetector; van der Waals

1 Introduction

Photodetectors can convert the absorbed optical signal into electrical signal[1], which are widely used in military reconnaissance[2], medical imaging[3], astronomy[4], optical communication[5], fire warning[6], temperature detection[7], *etc*. Based on the working mechanism, photodetectors can be categorized into photon detectors[8] and thermal detectors[9]. The thermal detectors can convert the infrared radiation energy induced by temperature change into electricity, which includes pneumatic detector[10], thermocouple[11], thermistor[12] and pyroelectric detector[13,14]. Thermal detectors can be used in fire alarming[15], temperature detection[16], rocket engine[17], thermal imaging[18], *etc*. However, their application is limited by temperature fluctuation noise arising from the radiating background. This drawback can be overcome by photon detectors[19]. Photon detectors are radiation detectors based on either external[2,20] or internal photoelectric effects[21,22](Fig. 1). Modern photodetectors are mostly based on the internal photoelectric effect, which are solid state electronic devices made of semiconductor materials and also known as semiconductor photodetectors[23]. In semiconductor photodetectors, two-dimensional (2D) material-based photodetectors[23] have attracted extensive interest because of their ultra-wide spectral response range from ultraviolet to terahertz, ultra-speedy photoresponsivity, and high spatial resolution for imaging[24].

The signal conversion process from optical signal to electrical signal in 2D material-based photodetectors can be separated into in 3 steps. (1) When the incident photons are absorbed by the photosensitive materials after the light trapping process, the photo-excited electrons transit from the valence band (VB) to the conduction band (CB) of the photosensitive materials and left holes in the VB. In this step, materials

Received date: 2024-01-31; **Revised date:** 2024-04-08
Corresponding author: GONG You-pin, Associate professor. E-mail: gongyp@cqu.edu.cn;
LIU Qing-feng, Professor. E-mail: qfliu@njtech.edu.cn;
CHEN Zhi-gang, Professor. E-mail: zhigang.chen@qut.edu.au
Author introduction: †ZHANG Xin-hua and LIU Wei-di contributed equally to this work
Homepage: http://xxtcl.sxicc.ac.cn/

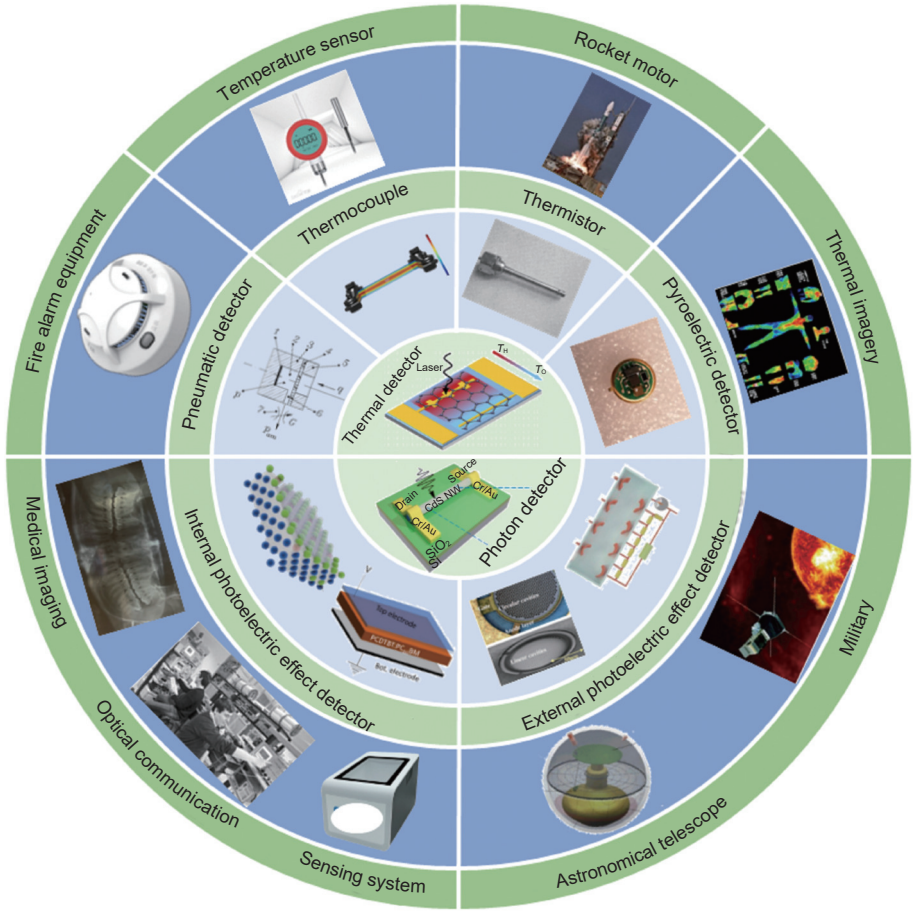

Fig. 1 Classification and applications of photodetectors[2,4,8-9,11,13,20-21,27-28]. Copyright, 2018, American Chemical Society[8]. Copyright, 2018, Springer Nature[9]. Copyright, 2020, The American Cheramic Society[13]. Copyright, 2020, CellPress[2]. Copyright, 2024, Elsevier[22]. Copyright, 2024, Elsevier[11]. Copyright, 2008, Elsevier[4]. Copyright, 2008, American Institute of Physics[20]. Copyright, 2020, Elsevier[21]. Copyright, 2008, Elsevier[27]. Copyright, 2008, Elsevier[28]

with high absorption coefficient and wide spectrum absorption range play important roles in improving the performance of 2D material-based photodetectors. (2) Under the applied external electric field or the internal electric field formed at the heterostructure interface, the photoinduced electron-hole pairs can be separated, and different carriers move to the corresponding electrodes along the conduction path. In this step, high carrier mobility (μ) of the material can contribute to high photoelectronic performance. (3) After the charge carriers arrive at the electrodes, in accordance with configurations of different electrodes, charge carriers can be extracted and conducted to the external circuit and generate the photocurrent[25]. Therefore, it can be seen that high-performance photodetectors require materials with high μ, high absorption coefficient, and wide spectrum absorption range[26].

Graphene, as one of the most important 2D layered materials, is a honeycomb crystal with a closed-packed hexagonal structure of single carbon atom[29–31]. Graphene has a Dirac conical belt structure with an ultrahigh μ of ~1 000 000 $cm^2\ V^{-1}\ s^{-1}$, which enables graphene having a high carrier collection rate and fast response time in graphene-based photodetectors[32–37]. Additionally, zero-band gap feature of graphene allows photo-generated carriers to transfer from the VB to the CB with nearly zero energy loss, and in turn fulfills the requirement of wide spectrum absorption range[38]. However, graphene has a very low light absorption (2.3%)[39] in the range from the ultraviolet to near-infrared region, which results in very fast interaction between light and the matter[40] and low detectivity (D^*) of only 2.2×10^8 Jones[41] in graphene-based 2D photodetectors.

To increase the D^* of graphene-based photodetectors, different photosensitive materials have been

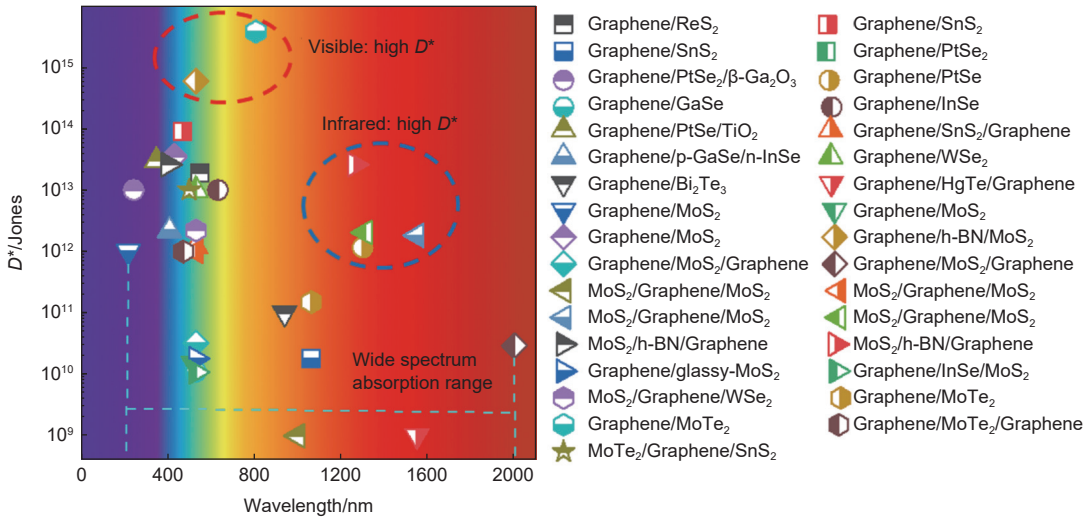

Fig. 2　Detectivity (D^*) of graphene-based 2D photodetectors based on van der Waals heterostructures (vdWHs) with different photosensitive materials, including graphene/ReS_2[45], graphene/SnS_2[46], graphene/$PtSe_2$[47], graphene/$PtSe_2$/β-Ga_2O_3[48], graphene/PbSe[49], graphene/GaSe[51], graphene/InSe[52], graphene/PbSe/TiO_2[50], graphene/$SnSe_2$/graphene[53], graphene/p-GaSe/n-InSe[54], graphene/WSe_2[55], graphene/Bi_2Te_3[56], graphene/HgTe/ graphene[57], graphene/MoS_2[58-60], graphene/h-BN/MoS_2[65], graphene/MoS_2/graphene[64], MoS_2/graphene/MoS_2[61,62], MoS_2/h-BN/graphene[66], graphene/glassy-MoS_2[63], graphene/InSe/MoS_2[67], MoS_2/graphene/WSe_2[68], graphene/$MoTe_2$[69], graphene/$MoTe_2$/graphene[70], $MoTe_2$ /graphene/SnS_2[71]

Table 1　Performance of graphene/photosensitive material-based photodetectors

Device structure	λ/nm	R/(mA·W^{-1})	τ_r/ms	τ_f/ms	D^*/Jones	Ref.
Graphene/ReS_2	550	1.0×10^{8}	30.0	30.0	1.9×10^{13}	[45]
Graphene/SnS_2	470 1064	7.7×10^{5} 2.0×10^{3}	–	–	8.9×10^{13} 1.8×10^{10}	[46]
Graphene/$PtSe_2$	1000	2.2×10^{2}	50.5	37.3	1.0×10^{7}	[47]
Graphene/$PtSe_2$/β-Ga_2O_3	245	76.2	1.2×10^{-3}	0.5	1.0×10^{13}	[48]
Graphene/PbSe	1300	6.6×10^{6}	50.0	175.0	1.2×10^{12}	[49]
Graphene/GaSe	532	3.5×10^{8}	10.0	10.0	1.1×10^{10}	[51]
Graphene/InSe	633	1.0×10^{8}	<0.1	<0.1	1.0×10^{13}	[52]
Graphene/PbSe/TiO_2	350	5.1×10^{2}	–	–	3.0×10^{13}	[50]
Graphene/$SnSe_2$/Graphene	532	1.3×10^{6}	30.2	27.2	1.2×10^{12}	[53]
Graphene/p-GaSe/n-InSe	410	2.1×10^{2}	0.6×10^{-2}	5.7×10^{-3}	2.2×10^{12}	[54]
Graphene/WSe_2	532	3.5×10^{5}	5×10^{-5}	3.0×10^{-2}	1.0×10^{13}	[55]
Graphene/Bi_2Te_3	940	1.0×10^{9}	–	–	1.0×10^{11}	[56]
Graphene/HgTe/ Graphene	1550	7.0	9.0×10^{-3}	0.7×10^{-3}	1.0×10^{9}	[57]
Graphene/MoS_2	220	3.3×10^{6}	–	–	1.0×10^{12}	[58]
Graphene/MoS_2	432	2.2×10^{8}	–	–	3.5×10^{13}	[59]
Graphene/MoS_2	520	2.1×10^{6}	–	–	1.5×10^{10}	[60]
Graphene/h-BN/MoS_2	532	3.6×10^{2}	–	–	5.9×10^{14}	[65]
Graphene/MoS_2/Graphene	532 2000	4.1×10^{5} 3.8×10^{5}	589.6	–	3.2×10^{10} 2.9×10^{10}	[64]
MoS_2/Graphene/ MoS_2	1000 532	–	–	–	1.0×10^{9} 1.0×10^{12}	[61]
MoS_2/Graphene/MoS_2	1550 1310	1.1×10^{2} 11.8	2.8×10^{-3}	4.7×10^{-2}	1.8×10^{12} 2.0×10^{12}	[62]
MoS_2/h-BN /Graphene	405 1265	1.8×10^{5} 1.5×10^{2}	230.0	2.5×10^{-2}	2.6×10^{13}	[66]
Graphene/glassy-MoS_2	532	12.3	–	–	1.8×10^{10}	[63]
Graphene/InSe/MoS_2	532	1.1×10^{2}	–	–	1.1×10^{10}	[67]
MoS_2/Graphene/WSe_2	532	4.3×10^{6}	5.4×10^{-2}	3.0×10^{-2}	2.2×10^{12}	[68]
Graphene/$MoTe_2$	1064 808	9.7×10^{5} 2.2×10^{4}	78.0	3.7×10^{2}	1.6×10^{11} 3.8×10^{15}	[69]
Graphene/$MoTe_2$/Graphene	473	8.7×10^{4}		23.0	1.0×10^{12}	[70]
$MoTe_2$ /Graphene/SnS_2	500	2.6×10^{6}	17.6	72.3	1.0×10^{13}	[71]

composited with graphene to form 2D van der Waals heterostructures (vdWHs)[42–44]. Fig. 2 and Table 1 summarize the performance of graphene-based photodetectors based on 2D vdWHs are formed with different photosensitive materials, including graphene/ReS_2[45], graphene/SnS_2[46], graphene/$PtSe_2$[47,48], graphene/PbSe[49,50], graphene/GaSe[51], graphene/InSe[52], graphene/$SnSe_2$/graphene[53], graphene/p-GaSe/n-InSe[54], graphene/WSe_2[55], graphene/Bi_2Te_3[56], graphene/HgTe/graphene[57], graphene/MoS_2[58–64], graphene/h-BN/MoS_2[65,66], graphene/InSe/MoS_2[67], MoS_2/graphene/WSe_2[68], graphene/$MoTe_2$[69,70], and $MoTe_2$/graphene/SnS_2[71]. As seen in Fig. 2, the graphene/MoX_2 vdWH photodetector has a wide absorption range from the ultraviolet (UV) to the infrared and a high D^* in the visible and infrared wavelength range. In the UV, the D^* of graphene/MoS_2 vdWH photodetectors can reach 1.0×10^{12} Jones. Graphene/$MoTe_2$ vdWH photodetector has a D^* of up to 3.8×10^{15} Jones, which is six orders of magnitude higher than other photodetectors. Graphene/$PtSe_2$/β-Ga_2O_3 vdWH photodetector can also detect light in the UV region. However, its responsivity (R) is low (76.2 mA W^{-1}) at 245 nm (Table 1). Although the detection capability of graphene/HgTe/graphene vdWH photodetector can be extended to the 1 550 nm near-infrared region, its performance is relatively weak with relatively low R (7.0 mA W^{-1}) and D^* (1.0×10^9 Jones) (Table 1). In contrast, the graphene/MoX_2 vdWH photodetectors have a wide spectrum absorption range from deep ultraviolet to mid-infrared region and approach the D^* as high as 3.8×10^{15} Jones. In the visible wavelength (λ) region, the D^* of graphene/MoX_2 vdWH photodetectors are at least an order of magnitude higher than other vdWH photodetectors. In the infrared region, the graphene/PtSe vdWH photodetector has a similar D^* and a relatively longer rise time (τ_r: 50 ms) and fall time (τ_f: 175 ms) which are also shown in Table 1. This can be attributed to the fact that 2D mono- and few-layer MoX_2 materials have high light absorption coefficient[72], which perfectly compensates for the drawbacks of graphene[73]. Therefore, MoX_2 is an extraordinary photosensitive material, and realize wide spectrum absorption range, high photocurrent and high responsivity (R) [74], which extends the applicability of graphene-based 2D vdWH photodetectors.

In this review, the advances in graphene/MoX_2 vdWH photodetectors are comprehensively overviewed. First, fundamental working principles, key performance indicators, and structures of photodetectors are summarized. Second, material crystal structures, electronic band structures and their relationship with photoelectronic performance are analyzed. After that, preparation methods of graphene/MoX_2 vdWH are summarized. In addition, the strategies for improving the photoelectric performance of graphene/MoX_2 vdWH photodetectors are reviewed. Applications of graphene/MoX_2 vdWH photodetectors are further overviewed based on the categorization of photodetectors. Finally, the challenges and prospects of graphene/MoX_2 vdWH photodetectors are pointed out.

2 Working principles

2.1 Photocurrent generation

Photocurrent in vdWH photodetectors can be generated by 3 effects, namely photoconductive effect[75–79], photothermoelectric effect[80–83] and photovoltaic effect[84–87]. Photoconductive effect, which is also known as photoelectric effect and photosensitivity effect, is the phenomenon that light causes the conductance change of semiconductor materials (Fig. 3a). Generally, the work function (W) of graphene (W_{Gr}) is ~4.6 eV, which can be tuned from 3.5 to 5.1 eV by external electric field or chemical doping[88–93]. Experimentally, the typical value of the W of MoX_2 (W_S) is 5.2–6.1 eV. The W_S of MoS_2, $MoSe_2$ and $MoTe_2$ are 6.1, 5.5 and 5.2 eV, respectively. Therefore, a metallic or intrinsic N-doped graphene contact with n-type MoX_2 (at this time $W_{Gr} < W_S$) would form ohmic contact (upper part of Fig. 3a) at the interface where electrons flow from the graphene into the lower energy states in MoX_2. When a bias voltage is applied to this graphene/MoX_2 junction under light, electrons can easily flow between graphene and MoX_2 depending on the direction of the bias, exhibiting a photocon-

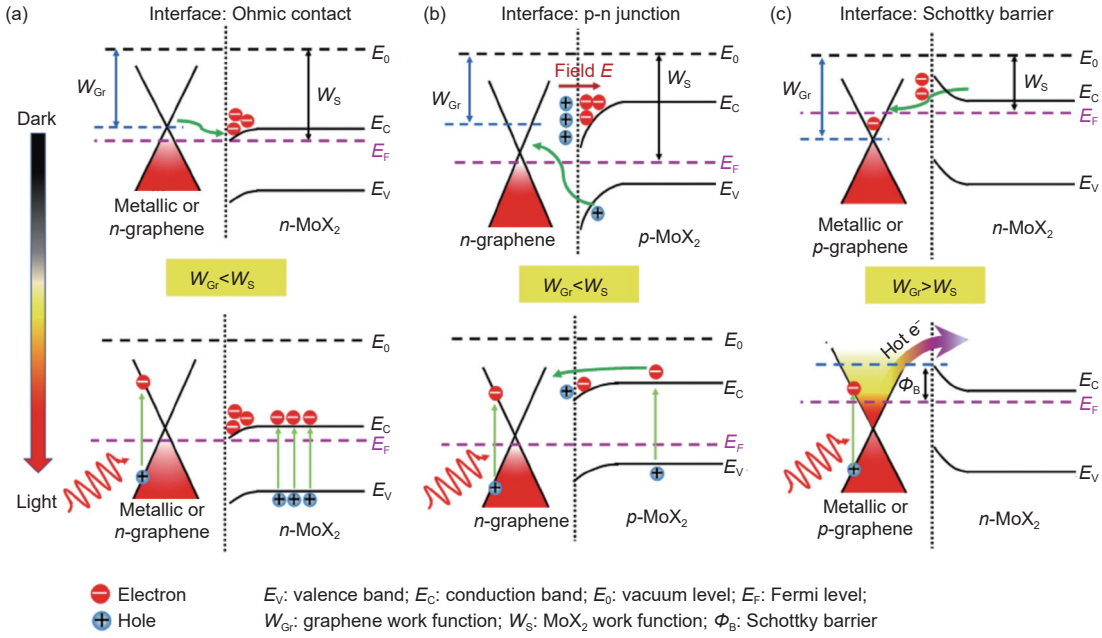

Fig. 3　Schematic band diagram of (a) photoconductive effect, (b) photovoltaic effect and (c) photothermoelectric effect at the graphene/molybdenum dihalide (MoX_2, X= S, Se and Te) interface. Upper and lower diagram represent the interface in the dark state and under the light, respectively

ductive effect (lower part of Fig. 3a), which is also the most common working mechanism of graphene/MoX_2 vdWH photodetectors[75–79]. Under this working principle, the device generally shows a large photoconductive gain. At the same time, it exhibits a large noise due to a large dark current (I), which results in a low D^*.

Photovoltaic effect refers to the phenomenon that light causes a potential difference between an uneven semiconductor, or between different parts of a semiconductor and a metal in Fig. 3b. Unlike ohmic contacts, when an n-type graphene is contacted with p-doped MoX_2 ($W_{Gr} < W_S$) to form a heterojunction, holes can diffuse from p-MoX_2 into graphene while electrons can diffuse from graphene into p-MoX_2 (upper part of Fig. 3b), which can cause the bands in p-MoX_2 to bend downward at the interface to form a p-n junction with a built-in potential barrier (or built-in electric field E). Such graphene/MoX_2 p-n heterojunctions exhibit the photovoltaic effect to enable self-powered photodetection under no bias, and also enable efficient exciton separation, which simultaneously leads to large R and D^* by applying a positive bias under light.

Photothermoelectric effect is a new photoelectric response mechanism, in which the hot carrier concentration and temperature gradient generated in the photoexcited materials can drive the carrier movement to form photocurrent as illustrated in Fig. 3c. When the W of p-doped graphene is larger than that of MoX_2 ($W_{Gr} > W_S$), the contact between graphene and MoX_2 will form a Schottky barrier (upper part in Fig. 3c), which is similar to the case that a semiconductor contacts with a metal. Basically, photons are absorbed by graphene to form electron-hole pairs during this process (lower part in Fig. 3c). These electron-hole pairs are rapidly balanced to form a hot carrier distribution, where a temperature gradient will form accordingly. As a result, the carrier energy is higher than the Schottky barrier formed at the graphene and MoX_2 interface, which can increase the carrier transfer rate between graphene and MoX_2, and form photocurrent[80].

2.2　Key performance indicators

High performance photodetectors require high response efficiency, fast response speed, and high response sensitivity. The R represents for the response efficiency of the overall photodetector, expressed by:

$$R = \frac{\text{Photocurrent}}{\text{Incident light power}} = \frac{I_{on} - I_{off}}{P_{in}} \quad (1)$$

where I_{on} is the light-on current, I_{off} is the dark current,

and P_{in} is the incident light power. Based on Eq. (1), when the P_{in} is a constant, the increase of photocurrent can induce the increase of R. G is photoconductive gain that is used to evaluate the efficiency of generating multiple carriers by a single incident photon, which can be defined as the capability to generate multiple carrier by a single incident photon[94], and expressed as:

$$G = \frac{\tau_{life}}{\tau_{transit}} \tag{2}$$

where τ_{life} is the lifetime of photoexciton, and $\tau_{transit}$ is the transit time to through channel. The $\tau_{transit}$ is dependent on the bias voltage (V_{bias}) applied at channel and the length of the channel (L), and given by[94]:

$$\tau_{transit} = \frac{L^2}{\mu V_{bias}} \tag{3}$$

Response speed can be evaluated by the response time (τ), where a lower τ indicates faster response speed. The τ is the sum of τ_r and τ_f. τ_r (τ_f) is defined as the time interval required for the response to rise (decay) from 10% (90%) to 90% (10%) of the net photocurrent peak. In photodetectors with fast response speed, photogenerated electron-hole pairs can be driven by the internal electric field to separate rapidly, which will induce low R as restricted by the maximum gain of unity[95].

Response sensitivity can be indexed by the D^*, external quantum efficiency (EQE), and internal quantum efficiency (IQE). D^* represents the sensitivity of photodetectors to weak signal, and can be expressed as:

$$D^* = \frac{\sqrt{AB}}{NEP} \tag{4}$$

where A is the effective area of photoelectric device, B is the electrical bandwidth, and NEP is the noise equivalent power. NEP is the minimum light signal power that can be detected from the total noise, which can be further categorized into thermal noise, shot noise and flicker noise. The NEP can be expressed as:

$$NEP = \frac{I_{noise}}{R} \tag{5}$$

where I_{noise} is the noise current spectra at 1 Hz bandwidth. From Eq. (4) and Eq. (5), it can be seen that the R and D^* are proportional[96]. EQE can reflect the sensitivity of photodetectors to collect photons. EQE is the ratio of the number of effective photoinduced carriers to the number of incident photons[97], which can be expressed as:

$$EQE = \frac{(I_{on} - I_{off})/e}{P_{in}/h\nu} = R\frac{hc}{e\lambda} \tag{6}$$

where e is the elementary charge, h is Planck's constant, ν is the frequency of incident light, c is the speed of incident light, and λ is the wavelength of incident light. Similarly, IQE can reflect the sensitivity of photodetectors to convert light into electrical energy. IQE is the ratio of the number of the electron-hole pairs which contribute to the photocurrent to the number of absorbed photons by the detector, and can be expressed as:

$$IQE = \frac{EQE}{\eta} \tag{7}$$

where η is the light absorption efficiency.

3 Photodetector structure

Fig. 4 shows the schematic structures of (a) lateral and (b) vertical graphene/MoX_2 vdWH photodetectors, which include a substrate (mesoporous Si with an

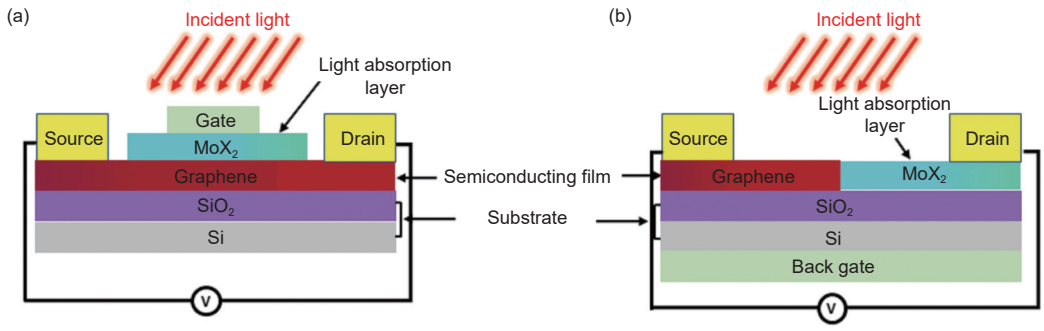

Fig. 4 Schematic structures of (a) lateral and (b) vertical graphene/molybdenum dihalide (MoX_2, X= S, Se and Te) van der Waals heterostructure photodetectors

additional amorphous bridging SiO_2 layer), a semiconducting film (graphene), a light absorption layer (MoX_2), and three gate/source/drain electrodes. In a graphene/MoX_2 vdWH photodetectors, the amorphous bridging SiO_2 layer is conducive to the deposition of graphene layers and can contribute to good structural stability[98]. High μ of graphene makes it a good candidate for the semiconducting film. Meanwhile, high light absorption coefficient of MoX_2 makes it a suitable light absorption layer[72]. The source/drain electrodes are typical Au/Ti or Au/Cr electrodes that are in direct and close contact with the graphene semiconducting film. The source and drain are in contact with graphene in a lateral structured graphene/MoX_2 vdWH photodetector (Fig. 4a). The source and drain are in contact with graphene and MoX_2, respectively, in a vertical heterojunction structured graphene/MoX_2 vdWH photodetector (Fig. 4b)[99]. The gate electrode can apply a vertical electric field to the graphene channel through a layer of insulating medium[100]. The photoelectronic performance is dominated by the structure and properties of the graphene/MoX_2 vdWH.

4　Fundamentals of graphene/MoX_2 vdWH

4.1　Crystal structures

Graphene, as the semiconducting layer of graphene/MoX_2 vdWH photodetectors, is a hexagonal honeycomb monolayer carbon crystal. Each protocell of graphene contains 2 carbon atoms. The distance between adjacent carbon atoms is 1.42 Å. Each carbon atom in graphene has 4 valence electrons. Three of the electrons form 3 bonds connecting 3 adjacent carbon atoms by sp^2 hybridization. The remaining orbital electrons of adjacent carbon atoms form a large π bond, which can move freely and contribute to the high μ of graphene[101] (Fig. 5a).

MoX_2, as the light absorption layer for graphene/MoX_2 vdWH photodetectors, is also a 2D layered material, in which each unit consists of 2 X atoms and one Mo atom. The MoX_2 layers are connected by weak van der Waals (vdWs) force, which make MoX_2 easily stripped into mono- or few-layer[72] (Fig. 5b). Mono- or few-layer MoX_2 mainly includes

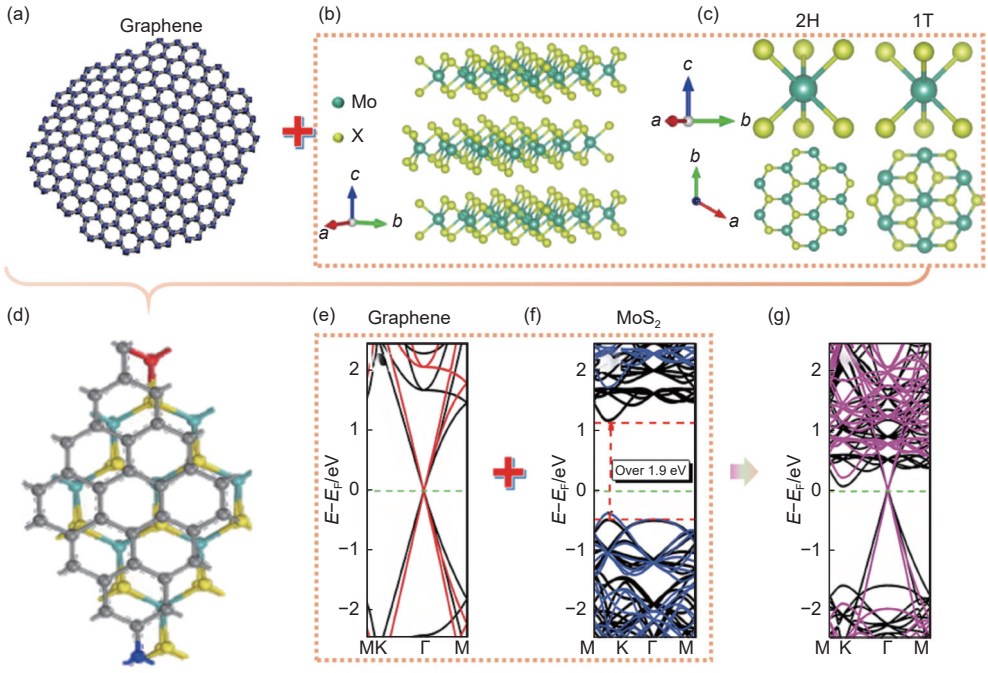

Fig. 5　(a) Graphene hexagonal honeycomb crystal structure. (b) 3D representation of the structure of molybdenum dihalide (MoX_2, X= S, Se and Te). (c) Crystal structures of MoX_2: including 2H and 1 T polytype. (d) Crystal structure of graphene/MoX_2 van der Waals heterostructure (vdWH). Copyright, 2015, Elsevier[106]. (e) Electron band structures of graphene, (f) MoS_2 and (g) graphene/MoS_2 vdWH at the equilibrium interfacial distance. The Fermi level (E_F) is set to zero and marked by green dotted lines. Black and color lines respectively for generalized gradient approximation of Per dew, Burke, and Engenho and HSE06 methods. Copyright, 2016, Royal Society of Chemistry[105]

the trigonal prismatic (1H) phase and the octahedral (1T) phase. As shown in Fig. 5c, in both 1H and 1T phases, each Mo atom is surrounded by 6 X atoms. With the offset of X atoms in the upper and lower planes, the 1H phase is arranged in a prism-like coordination. Meanwhile, the 1T phase is arranged in an octahedron coordination. The different atomic arrangements in 1H and 1T phases are dominated by the atom count of the 4d orbitals of Mo, where filled orbitals induce semiconducting behavior and the formation of 1H-phase MoX_2. And partially filled 4d orbitals of Mo induce metallic behavior the formation of metallic 1T-phase MoX_2[102]. Therefore, the metallic 1T-phase MoX_2 exhibits high μ due to partial filling of the Mo 4d orbitals. In contrast, the 1H-phase MoX_2 exhibits high photon absorption derived from the semiconducting behavior, which can effectively improve the performance of photodetectors[103].

2D graphene and MoX_2 can easily form a vdWH by forming weak vdWs force between the 2D graphene layers and 2D mono- or few-MoX_2 layers (Fig. 5d). Such a vdWH can achieve charge transfer and separation between layers. Graphene/MoX_2 vdWH can realize tight connection between the graphene and MoX_2 layers and contribute to suitable band manipulation at the graphene/MoX_2 interfaces. Therefore, graphene/MoX_2 vdWH can realize effective utilization of the unique optoelectrical properties of graphene and MoX_2, and have demonstrated good optical, electrical, thermal, and electromagnetic properties, which can be widely used in the field of optoelectronics.

4.2 Electronic band structures

As illustrated in Fig. 5e, the band structure of graphene satisfies the linear dispersion relationship, where the CB and VB meet at the Dirac point and form a zero-band-gap band structure[69]. Zero-band gap graphene has the advantages of high μ, wide spectral absorption range, and high transmittance. However, the high transmittance results in high dark current in graphene-based photodetectors[41], which can be overcome by forming graphene/MoX_2 vdWH. Generally, monolayer MoX_2 has a direct bandgap and high absorption coefficient. Taking monolayer MoS_2, as an example as illustrated in Fig. 5f, monolayer MoS_2 is a direct band-gap semiconductor with a bandgap of ~1.9 eV, leading to a high absorption coefficient of 2.8×10^6 cm^{-1}[104]. Fig. 5g schematically shows the electronic band structure of a graphene/MoS_2 vdWH, which combines the electronic band structure features of both graphene and MoS_2, leading to simultaneously high μ and absorption coefficient[105].

5 Preparation methods of graphene/MoX_2 vdWH

Graphene/MoX_2 vdWH can be successfully prepared by wet transfer[107], dry transfer[108], inkjet printing[109,110] and successive deposition[111](Fig. 6). As summarized in Table 2, wet transfer methods, as the most widely used preparation methods, can induce high R (4.3×10^6 mAW^{-1}) and D^*(3.8×10^{15} Jones). During wet transfer processes, polymers (such as polymethyl methacrylate (PMMA)[112], poly(L-lactic acid)[113], polystyrene[114] and polyvinyl alcohol) are typically employed as a protective layer for 2D materials. PMMA is currently the most widely used protective layer in the laboratory because it is easy to fabricate and remove[112]. The schematic process of wet transfer is presented in Fig. 6a, where the 2D material grown on the metal substrate is firstly spin-coated with PMMA film. Then, it is heated for the purpose of curing, and placed into the etching solution to etch the metal substrate. After further drying, the 2D material/PMMA composite will be transferred on the

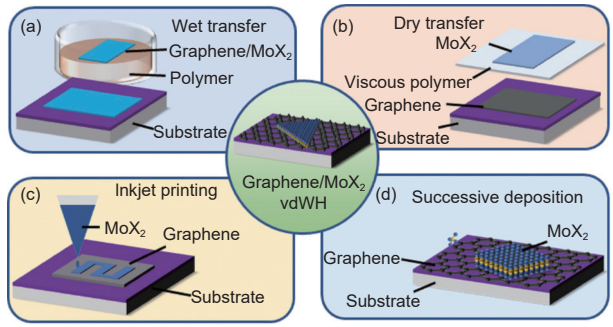

Fig. 6 Preparation methods of graphene/molybdenum dihalide (MoX_2, X= S, Se and Te) van der Waals heterostructures

Table 2　Synthesis and performance of typical graphene/molybdenum dihalide (MoX_2, X = S, Se and Te) van der Waals heterostructure (vdWH) photodetectors

Device structure	Synthesis of graphene/MoX_2	λ/nm	R/(mA·W^{-1})	D^*/Jones	τ_r /ms	τ_f /ms	EQE	Ref.
h-BN/$MoTe_2$/Graphene /SnS_2/h-BN	Dry transfer	500	2.6×10^6	1.0×10^{13}	17.6	72.3	10^6 to 10^5	[71]
MoS_2/h-BN /Graphene	Dry transfer	405	1.8×10^5	2.6×10^{13}	230	250.0	–	[66]
Graphene/InSe/MoS_2	Dry transfer	532	110	1.1×10^{10}	–	–	25.7%	[67]
MoS_2/Graphene/MoS_2	Dry transfer	1000 532	–	1.0×10^9 1.0×10^{12}	–	–	55%	[61]
Graphene/$MoTe_2$/Graphene	Dry transfer	473	8.7×10^4	1.0×10^{12}	–	23.0	–	[70]
Graphene/$MoTe_2$	Wet transfer	1064	9.7×10^5	1.6×10^{11}	78	375.0	–	[53]
MoS_2/Graphene/MoS_2	Wet transfer	808 1550 1310	2.2×10^4 10.6 11.8	3.8×10^{15} 1.8×10^{12} 2.0×10^{12}	2.8×10^{-3}	4.7×10^{-2}	–	[62]
MoS_2/Graphene/WSe_2	Wet transfer	532	4.3×10^6	2.2×10^{12}	5.3×10^{-2}	3.0×10^{-2}	1×10^6%	[68]
Graphene/$MoTe_2$	Wet transfer	1265 1300 1330	1.5×10^2 50 20	–	19	–	20%	[122]
Graphene/$MoTe_2$/Graphene	Wet transfer	1064 473	110 205	–	2.4×10^{-2}	4.6×10^{-2}	12.9% 53.8%	[123]
Graphene/MoS_2/WS_2	Wet transfer	400 1550	6.6×10^{10} 1.7×10^4	–	21.9	7.0	13.7%	[124]
Graphene/MoS_2/Graphene	Wet transfer	532 2000	4.1×10^5 3.8×10^5	3.2×10^{10} 2.9×10^{10}	589.6	–	9.7×10^4% 2.3×10^4%	[64]
Graphene/MoS_2	Wet transfer	220	3.4×10^6	1.0×10^{12}	–	–	1.8×10^4	[58]
Graphene/MoS_2	Wet transfer	520	2.1×10^6	1.5×10^{10}	–	–	–	[60]
Graphene/h-BN/MoS_2	Wet transfer	532	3.6×10^2	5.9×10^{14}	–	–	80%	[65]
Graphene/glassy-MoS_2	Wet transfer	532	12.3	1.8×10^{10}	–	–	–	[63]
Graphene/MoS_2	Inkjet printing	540	8.4×10^5	–	20	30	–	[125]
Graphene/MoS_2	Successive deposition	532	2.4×10^3	–	–	–	–	[111]
Graphene/MoS_2	Successive deposition	432	2.2×10^8	3.5×10^{13}	–	–	–	[59]

target substrate, where the PMMA can be removed by acetone cleaning[115]. However, the introduction of PMMA inevitably deteriorates the cleanliness of the vdWs interface, increases the complexity, and slows down the process of spin coating and heating[116].

Dry transfer methods rely on viscous polymers to transfer an arbitrary 2D material to the surface of another one (Fig. 6b). In dry transfer processes, complex sub-steps (rotating coating and heating) can be excluded, and corresponding interface contamination can be avoided. Although this dry transfer method is very popular in experimental research, it is difficult to apply to large-area 2D materials, and also meet the requirements of mass-fabricated devices. Moreover, these dry transfer process induces additional external strain and influences the uniformity of 2D materials[116]. Therefore, it is very important to choose appropriate polymer media and avoid significant influence on the uniformity of as-prepared 2D graphene/MoX_2 vdWH[71].

Other than wet and dry transfer methods, inkjet printing can be used to fabricate graphene/MoX_2 vdWH by directly printing the materials layer by layer (Fig. 6c), resulting in the clean vdWs interface and the high R, $D^*$and low τ. However, to facilitate printing, 2D nanosheets dispersed in inks need to be as small as possible. The small surface area of 2D nanosheets dispersed in the ink can introduce dense grain boundaries in the film, hinder the transport of charge carriers, and reduce the R of photodetectors[110].

Successive deposition is cycling the deposition for twice to prepare heterostructures (Fig. 6d). Deposition methods, including chemical vapor deposition (CVD)[117,118], physical vapor deposition[119], electron beam evaporation[120], and magnetron sputtering[121], can be used to effectively prepare large area and high quality 2D materials. Among various deposition methods, CVD method is the most used due to its simplicity, fast growth rate, and cost-effectiveness. CVD is a process that uses gaseous substances to react in the gas phase or gas-solid interface to form solid-state products[118]. However, during CVD process, growth

temperature and precursors have significant influence on the size and quality of the products.

6 Performance-engineering strategies

6.1 Interface cleaning

A clean interface in heterostructures can reduce the amount of charge traps, contribute to efficient transfer of photo-generated carriers, enhance the photocurrent, and thus improve the *R* of the photodetectors. Facile wet transfer methods are widely used for the preparation of graphene/MoX_2 vdWH, which inevitably produce contamination at the interface in the graphene/MoX_2. Fig. 7a is a transmission electron microscope (TEM) image showing the interface in a typical graphene/MoS_2 vdWH. Apparently, the transferred graphene is not uniform and can only partially cover the MoX_2, where the rest of the interface is contaminated. To solve this problem, Liu et al.[125] used an inkjet printing method to prepare a graphene/MoS_2 vdWH as schematically shown in Fig. 7b. This process is transfer-free and can maintain a clean interface between graphene and MoS_2. Fig. 7c shows low-magnification atomic force microscope (AFM) image of the 2D film of graphene/MoS_2 vdWH, where over 80% of MoS_2 layer (thickness of ~0.7 nm) is fully covered by graphene. As shown in Fig. 7d, the clean vdWs interface helps to facilitate the transfer of photogenerated holes from MoS_2 to graphene. The photogenerated holes transferred into graphene can be driven by the applied bias voltage (V_{DS}) to cycle through the external circuit many times until they combine with the photogenerated electrons in the MoS_2 layer, resulting in a highly *R* photodetector. In Fig. 7e, the photocurrent of transfer-free graphene/MoS_2 vdWH photodetector is increased by about 22 times compared with that prepared by the wet transfer method

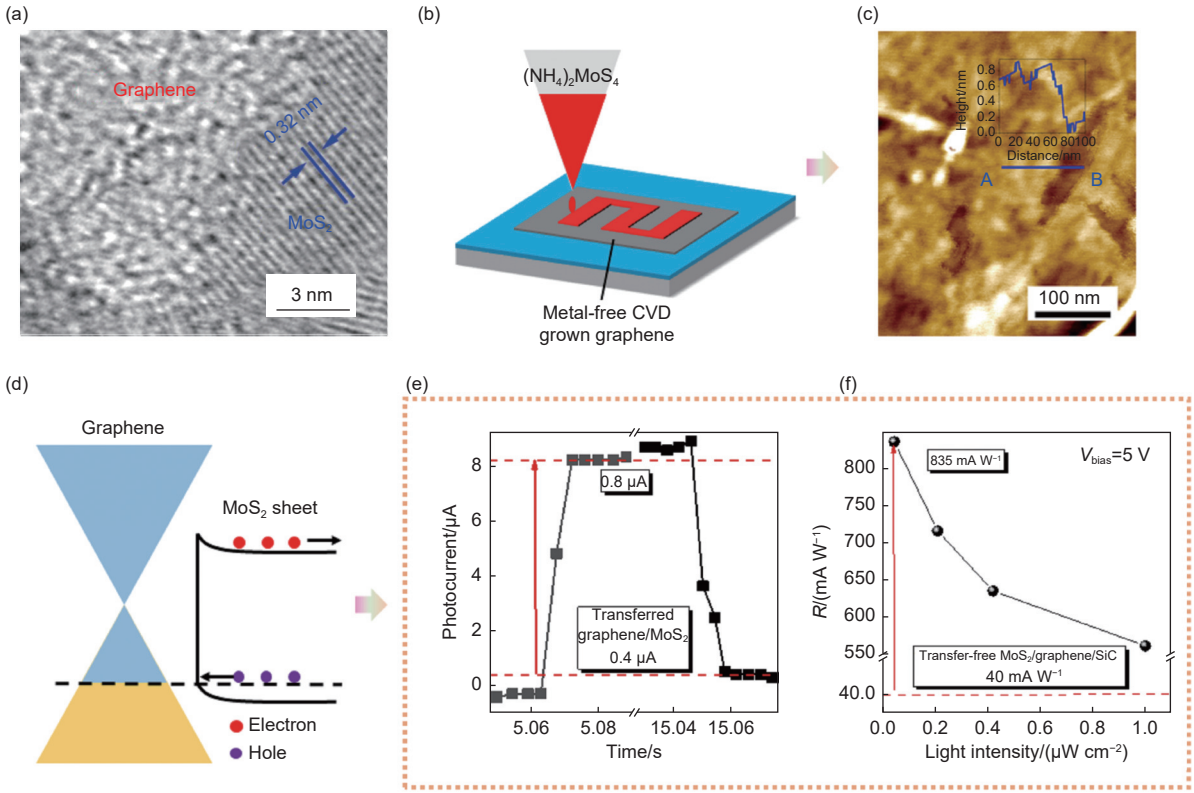

Fig. 7 (a) Transmission electron microscope (TEM) image of the transferred graphene/MoS_2 van der Waals heterostructure (vdWH. Copyright, 2017, American Chemical Society)[125]. (b) Schematic fabrication process of the transfer-free graphene/MoS_2 vdWH. (c) Atomic force microscope (AFM) image of the transfer-free graphene/MoS_2 vdWH. Copyright, 2017, American Chemical Society[125]. (d) Schematic diagram of the transfer-free graphene/MoS_2 interface band. Copyright, 2017, American Chemical Society[125]. (e) Comparison of time-dependent photocurrent of the transfer-free graphene/MoS_2 and transferred graphene/MoS_2. Copyright, 2017, American Chemical Society[125]. (f) Comparison of responsivity (*R*) of the transfer-free graphene/MoS_2 and trans-free MoS_2/graphene/SiC. Copyright, 2017, American Chemical Society[125]

under the same condition due to a clean graphene/MoS_2 vdWs interface. Correspondingly, the R of transfer-free graphene/MoS_2 vdWH prepared by inkjet printing with a clean vdWs interface is 20 times higher than that of transfer-free MoS_2/graphene/SiC (Fig. 7f). After introducing a clean vdWs interface, a high R of 835 mA W^{-1} has been approached in the transfer-free graphene/MoS_2 vdWH photodetector.

6.2 Blocking interlayer coupling

During separation process of photogenerated electron-hole pairs, photo-generated holes can be easily consumed by interlayer coupling formed during the graphene and MoX_2 stacking process[107,126]. Taking a graphene/MoS_2 vdWH photodetector as an example, as schematically shown in Fig. 8a, blocking the interlayer coupling can avoid the consumption of diffusion of photogenerated holes into graphene, effectively accelerate carrier migration and enhance the photocurrent of graphene/MoX_2 vdWH. To realize this purpose, Li et al.[65] introduced an atomically thin hexagonal boron nitride (h-BN) film into the graphene/MoS_2 interface in Fig. 8b. Fig. 8c shows the photoluminescence (PL) intensities of pristine MoS_2, graphene/MoS_2 and graphene/MoS_2/h-BN vdWH as a function of the incident light wavelength. As can be seen, after forming graphene/MoS_2 vdWH, due to the interlayer coupling at graphene/MoS_2 vdWs interface, the PL peak intensity is reduced. After further insertion of h-BN, the interlayer coupling between graphene and MoS_2 is blocked, leading to an increased PL peak intensity. This is mainly because the interlayer carrier recombination at the graphene/MoS_2 interface is effectively blocked by the inserted h-BN. Meanwhile, the photogenerated holes can achieve interlayer transport through quantum tunneling, contributing to the effective restoration of the photovoltaic effect. Fig. 8d compares I-V_{DS} curves of the MoS_2/graphene and MoS_2/h-BN/graphene vdWH photodetectors under dark and illumination conditions. Impressively, the photocurrent increases significantly after the insertion of h-BN due to the restoration of the photovoltaic effect at the V_{DS} of 0 V, while the electrical behaviors of the photodetectors are similar before and after insertion of h-BN at higher V_{DS}. The

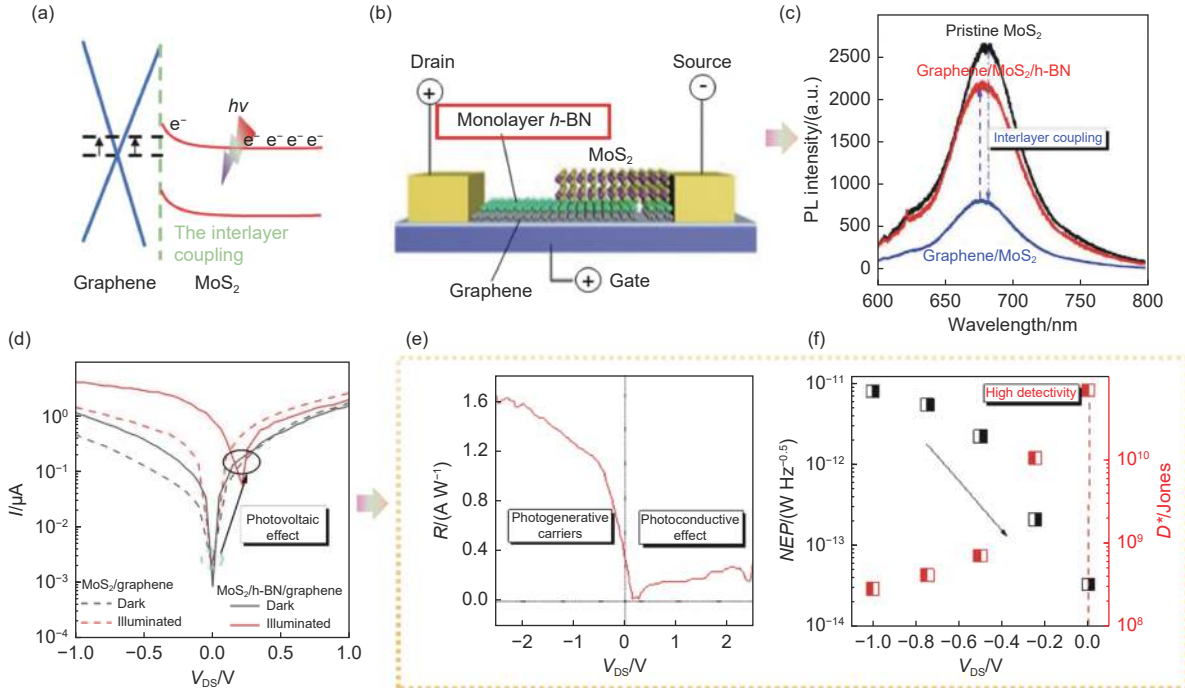

Fig. 8　(a) Schematic band diagram of graphene/MoS_2. (b) Schematic of the graphene/MoS_2/h-BN van der Waals heterostructure (vdWH) device. Copyright, 2018, Elsevier[65]. (c) Comparison of the photoluminescence (PL) intensities of pristine MoS_2, graphene/MoS_2 and graphene/MoS_2/h-BN. Copyright, 2018, Elsevier[65]. (d) Comparison of current- bias voltage (I-V_{DS}) curves of the graphene/MoS_2 and graphene/MoS_2/h-BN vdWH photodetectors in dark and light illumination. (e) Responsivity (R) of photodetector versus V_{DS}. Copyright, 2018, Elsevier[65]. (f) Noise equivalent power (NEP) and detectivity (D^*) of the graphene/MoS_2 photodetector versus V_{DS}

restoration of photovoltaic effect is conducive to the improvement of response efficiency and response sensitivity of a photodetector. As shown in Fig. 8e, under positive V_{DS}, the photocurrent mainly comes from the photoconductive effect. At zero and negative V_{DS}, the electric field in MoS_2/h-BN/graphene vdWH photodetector generates many photo-generated carriers, contributing to a high R. Based on Eq. (4) and Eq. (3), the increase in R leads to a decrease in NEP and an increase in D^*. Compared with photodetectors working under negative V_{DS}, NEP and corresponding D^* are significantly improved under zero V_{DS}, as shown in Fig. 8f. Obviously, inserting h-BN to block interlayer coupling can effectively improve the R and D^* of the photodetectors.

6.3 Internal electric field construction

Internal electric field can drive the photogenerated electron-hole pairs in MoX_2 through the graphene channel, improve the value of μ and enhance the photocurrent of the photodetectors[127] as schematically shown in Fig. 9a. For example, Li et al.[86] used asymmetric metal contacts (titanium and palladium) to provide a strong internal electric field as compared with symmetric metal contacts. In Fig. 9b, when symmetric metal contacts are used, the photocurrent and dark current curves intersect at the point where V_{DS}= 0 mV, indicating that there is no internal electric field. In contrast, while asymmetric metal contacts are used, a strong internal electric field of 110 mV can be observed, as indicated by the shift of zero photocurrent point in Fig. 9c. The large internal electric field results in a high photocurrent (~ 0.225 μA) and correspondingly an increased R (~ 3 A/W) as shown in Fig. 9d. While the detector is operated with asymmetric metal contacts at V_{DS}=0 V, a low dark current of only 0.9 nA (as compared with 17.25 μA of the photodetector with symmetric metal contacts) and a high I_{on}/I_{off} ratio of up to 1 428 (as compared with 1.11 of the photodetector with symmetric metal contacts) can be obtained (Fig. 9e). An enlargement of Fig. 9e

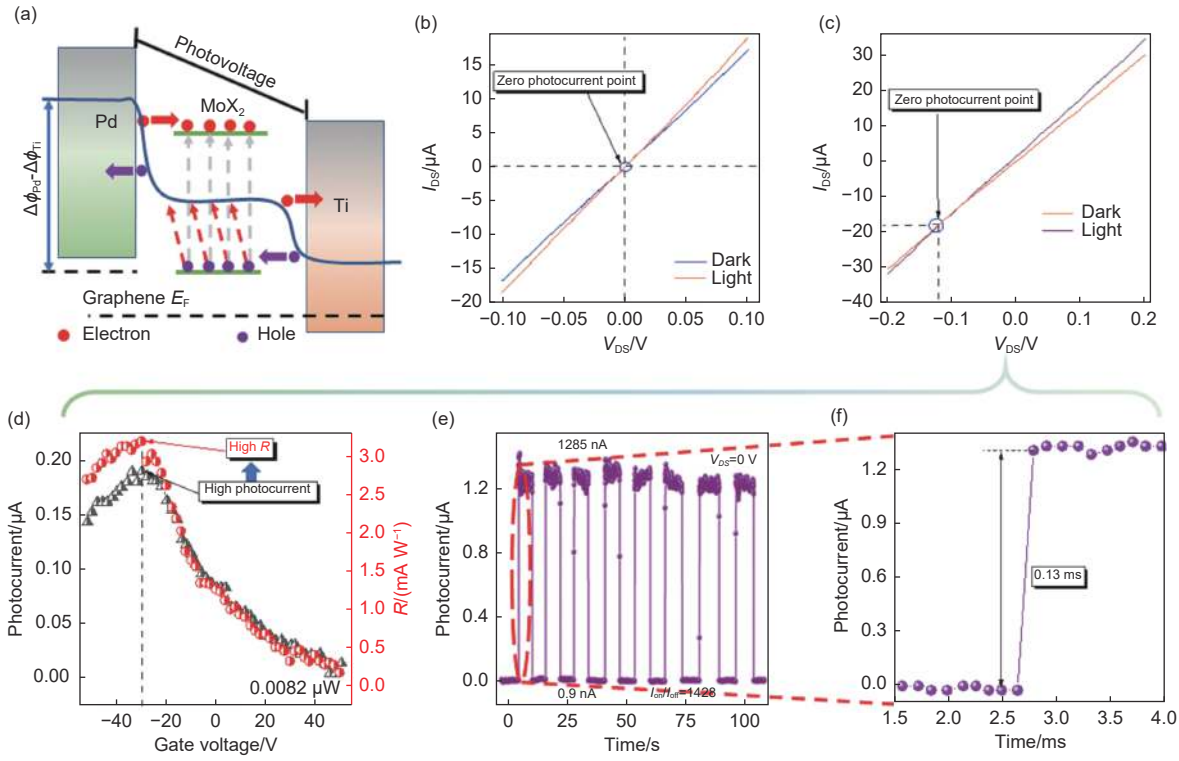

Fig. 9 (a) Energy diagram of the graphene/molybdenum dihalide (MoX_2, X= S, Se and Te) hybrid photodetector with asymmetry metal contact under light irradiation. $\Delta\varphi_{Pd}$ and $\Delta\varphi_{Ti}$ represent the difference between the Dirac point energy and the Fermi level (E_F) in palladium- and titanium-doped graphene, respectively. Copyright, 2020, American Chemical Society[86]. (b) Difference of current (I) between Dirac point energy and E_F in graphene under symmetric metal contact. (c) Difference of I between Dirac point energy and E_F in graphene under asymmetry metal contact. (d) Curve of photocurrent and responsivity (R) with gate voltage under asymmetric metal contact. (e) Photocurrent response of graphene/MoS_2 phototransistor with asymmetric metal contact. Copyright, 2020, American Chemical Society[86]. (f) Corresponding enlarged figures of (e). Copyright, 2020, American Chemical Society[86]

shows that the τ_r of the photodetector is only 0.13 ms (Fig. 9f), which is 217 times smaller than that of the photodetector with symmetric metal contacts.

6.4 Schottky barrier removal

As the work function of graphene (4.3 eV) is close to the electron affinity of MoS_2 (4.2 eV), a Schottky barrier exists at the graphene/MoX_2 interface of graphene/MoX_2 vdWH[105]. Although in the mentioned photothermoelectric effect, the presence of Schottky barrier in the contact of graphene with MoX_2 does not cause obstacles to emission of hot electrons, the Schottky barrier will prevent the migration of photo-generated carriers in the photoconductive and photovoltaic devices. Therefore, reducing the Schottky barrier can allow more photo-generated holes transit from MoX_2 to graphene and generate higher photocurrent[128]. Lee et al.[59] fabricated a gate using graphene, which can modulate the Schottky barrier by adjusting the gate bias (V_{gs}) as schematically shown in Fig. 10a[59]. Fig. 10b schematically shows that upon illumination, the photo-generated electrons can further raise the E_F of graphene, resulting in a lower Schottky barrier in the graphene/MoS_2 vdWH. While applying high voltage on the structure, the Schottky barrier can be measured by the Fowler-Nordheim tunneling (FNT) model, which can be expressed as[66]:

$$I_{FNT} = \frac{Aq^3 m V_{DS}^2}{8\pi h \phi_{SBH} d^2 m^*} \exp\left[\frac{-8\pi\sqrt{2m^*}\phi_{SBH}^{3/2} d}{3hqV_{DS}}\right] \quad (8)$$

where A, q, m, h, ϕ_{SBH}, d, m^* are effective contact area, electron charge, free electron mass, Planck constant, Schottky barrier height, barrier width, effective electron mass, respectively. For ease of calculation, Eq. (8) can then be converted into

$$ln\left(\frac{I_{FNT}}{V_{DS}^2}\right) = ln\left(\frac{Aq^3 m V_{DS}^2}{8\pi h \phi_{SBH} d^2 m^*}\right) - \frac{8\pi\sqrt{2m^*}\phi_{SBH}^{3/2} d}{3hqV_{DS}} \quad (9)$$

Fig. 10c presents the variation curve of $ln(1/V_{DS}^2)$ with $1/V_{DS}$, where the height of the Schottky barrier can be evaluated by the negative slope. Obviously, the effective Schottky barrier disappears when V_{gs} = −3 V at the incident power of 0.14 μW. When the positive gate bias (V_{gs}) is sufficiently high compared with the threshold voltage (V_{th}), the graphene is doped by the photo-generated hole (Fig. 10d). However, since the Schottky barrier has been removed, the photocurrent

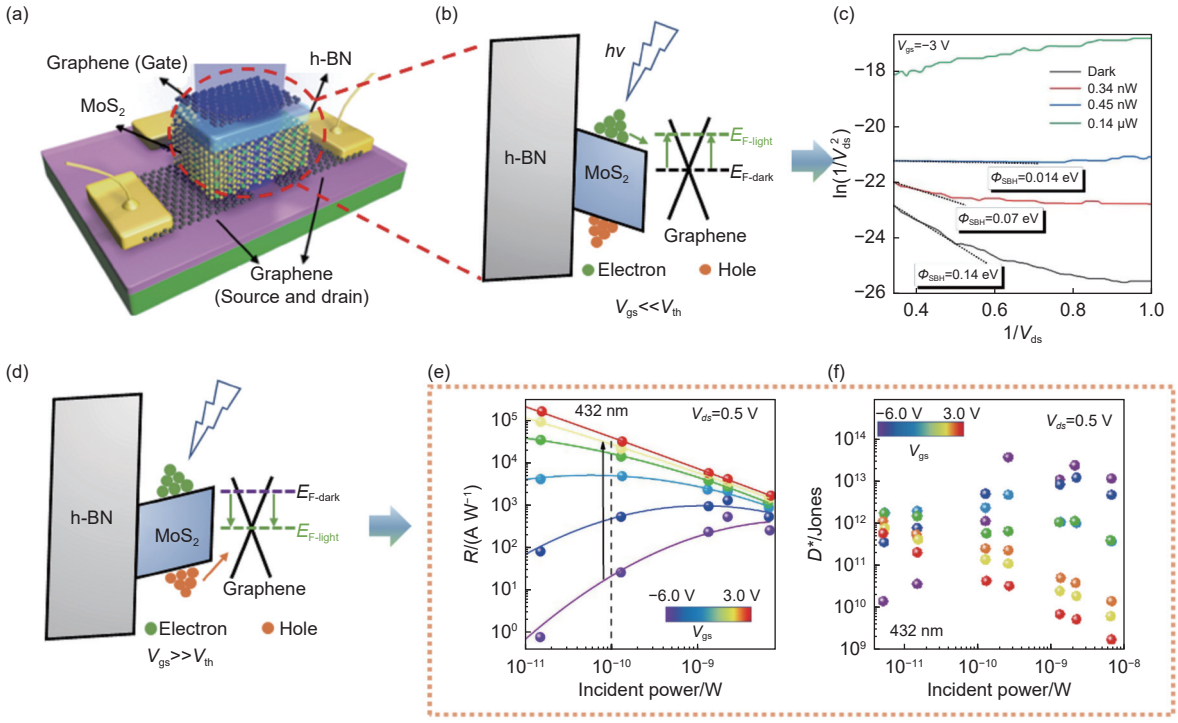

Fig. 10　(a) Schematic image of the MoS_2 photodetector with graphene gate electrode. Copyright, 2020, American Chemical Society[59]. (b) Band diagram of vertical direction of the device (gate bias (V_{gs}) << threshold voltage (V_{th})). (c) Fowler-Nordheim tunneling (FNT) plots at different incident powers. (d) Band diagram of vertical direction of the device (V_{gs} >> V_{th}). (e) Responsivity (R) depending on effective incident power at different V_{gs}. Copyright, 2020, American Chemical Society[59]. (f) Detectivity (D^*) depending on effective incident power at different V_{gs}. Copyright, 2020, American Chemical Society[59]

can flow smoothly, contributing to high R and D^*. Fig. 10e and f compare the changes in R and D^* at different V_{gs} and incident optical powers. When the V_{gs} is in the range of −2 to 3 V, the R and D^* decreases with increasing the incident power. However, when the V_{gs} is in the range of −6 to −3 V, the R and D^* increases with increasing the incident power. Under a fixed incident power, with increasing the V_{gs}, the R and D^* also increase. The R and D^* can reach 2.2×10^5 mA W^{-1} and 3.5×10^{13} Jones, respectively. Therefore, reducing the Schottky barrier can effectively boost the migration of photogenerated holes and enhance photocurrent, R and D^* of a photodetector.

7 Conclusions and outlook

Graphene/MoX_2 vdWH photodetectors simultaneously possess high μ, wide spectral absorption range, and high contact quality with the electrodes, which has been widely applied in modern electronics. In this paper, a comprehensive review of graphene/MoX_2 vdWH photodetectors are presented. After introducing the fundamental principles, key performance indicators and structure of corresponding graphene/MoX_2 vdWH photodetectors, the fundamentals of the graphene/MoX_2 vdWH photodetector is summarized. Then, typical preparation methods of graphene/MoX_2 vdWHs are summarized, including wet transfer, dry transfer, inkjet printing and successive deposition methods, with corresponding performance discussion. Among these methods, wet transfer is the most commonly used one, but this method inevitably leads to contamination of the vdWs interface. Dry transfer and inkjet printing methods can keep the vdWs interface clean, but correspondingly introduce external strains and grain boundaries that reduce the performance of the photodetector. Successive deposition methods can maintain the cleanliness of the vdWs interface without introducing external strains and grain boundaries by avoiding the transfer process of graphene. However, it is complicated, time-consuming, and costly. Finally, the strategies for regulating the performance of graphene/MoX_2 vdWH photodetectors are overviewed from 4 aspects: interface cleaning, blocking interlayer coupling, internal electric field construction and Schottky barrier removal. Interface cleaning and internal electric field construction facilitates the transfer of photogenerated carriers to improve photodetector performance. Blocking interlayer coupling and Schottky barrier removal help to avoid the consumption of photogenerated holes thus accelerating μ and enhancing photocurrent.

With the significant development of photodetectors, including both preparation methodologies and performance enhancement strategies, a high R of 6.6×10^{10} mA/W has been approached in a graphene/MoS_2/WS_2 vdWH photodetector[124]. Additionally, D^* has also approached as high as 3.8×10^{15} Jones, and the τ has reduced to as low as 0.049 4 ms in a MoS_2/graphene/MoS_2 vdWH photodetector[62]. However, some key challenges remain to be further overcome:

(1) From the performance viewpoint, it is of great significance to approach high response efficiency, high response sensitivity, and fast response speed to meet the needs of different applications. For example, high R plays an important role in the application of imaging, which also requires low *NEP* and low energy consumption.

(2) High quality graphene is foundation for high sensitivity photodetector. High-quality (device-quality) graphene refers to monolayer or few layers graphene with low roughness, defect-free and high purity. However, graphene in photodetectors is mostly prepared by wet transfer and dry transfer methods, where organic residue or other contaminants are inevitable, leading to low quality of graphene. Therefore, the μ of graphene in practical device applications is relatively low, resulting in low sensitivity and high-power consumption. To address these issues, more facile, and cost-effective inkjet printing and successive deposition are worth investigating to prepare high-performance graphene/MoX_2 vdWH photodetectors.

(3) Maintaining the vdWH interface clean is necessary to improve the performance of photodetectors. During the current assembly process, the residue contamination of the interface affects the generation of excitons and the transport of carriers, which leads to the degradation of the detector performance. Al-

though the inkjet printing method can effectively address this problem, the introduced dense grain boundaries hinder the transport of charge carriers and reduce the performance of the photodetector. Therefore, searching new appropriate way to maintain clean vdWH interface remains a significant challenge.

(4) 2D materials tend to adsorb water and oxygen molecules in air, especially compounds of Se and Te, which deteriorates the performance of photodetectors, for example, reducing their response speed and stability. It is therefore important and urgent for future practical applications to seek a suitable packaging materials and process for 2D photodetection devices in order to ensure the reliability of the devices without compromising their performance.

Conflict of Interest

The authors declare no conflict of interest.

Acknowledgements

This work was financially supported by the National Natural Science Foundation of China (51972170), the State Key Laboratory of Materials-Oriented Chemical Engineering (SKL-MCE-23A04), the Priority Academic Program Development of Jiangsu Higher Education Institutions (PAPD), and the Jiangsu Specially-Appointed Professor Program. CHEN Zhi-gang thanks the financial support from the Australian Research Council, and QUT Capacity Building Professor Program. GONG You-pin acknowledges support from the Chongqing Research Program of Basic Research and Frontier Technology (cstc2021jcyj-msxmX0641) and the Doctoral "through train" scientific research project of Chongqing (CSTB2022BSXM-JCX0085).

References

[1] Koppens F H L, Mueller T, Avouris P, et al. Photodetectors based on graphene, other two-dimensional materials and hybrid systems[J]. Nature Nanotechnology, 2014, 9(10): 780-793.

[2] Zheng W, Jia L M, Huang F. Vacuum-ultraviolet photon detections[J]. iScience, 2020, 23(6): 22.

[3] Ji F, Kalliopuska J, Eranen S, et al. Via-in-pixel design of truly 2D extendable photodiode detector for medical CT imaging [J]. Sensors and Actuators A-physical, 2008, 14559-65.

[4] Lubsandorzhiev B K. The quest for the ideal photodetector for the next generation deep-underwater neutrino telescopes[J]. Nuclear Instruments and Methods in Physics Research-section A, 2008, 595(1): 58-61.

[5] Hu J J, Li L, Lin H T, et al. Flexible integrated photonics: Where materials, mechanics and optics meet Invited[J]. Optical Materials Express, 2013, 3(9): 1313-1331.

[6] Qu Z C, Xu C A, Li X B, et al. Facile preparation of BP-MoS_2/GO composite films with excellent flame retardancy and ultrasensitive response for smart fire alarm [J]. Chemical Engineering Journal, 2021, 426130717.

[7] Li X, Wang J, Xie D, et al. Reduced graphene oxide/MoS_2 hybrid films for room-temperature formaldehyde detection [J]. Materials Letters, 2017, 18942-45.

[8] Luo W, Weng Q, Long M, et al. Room-temperature single-photon detector based on single nanowire[J]. Nano Letters, 2018, 18(9): 5439-5445.

[9] Shautsova V, Sidiropoulos T, Xiao X, et al. Plasmon induced thermoelectric effect in graphene[J]. Nature Communications, 2018, 9(1): 5190.

[10] Belforte G, Raparelli T, Viktorov V, et al. Theoretical and experimental investigations of an opto-pneumatic detector[J]. Journal of Dynamic Systems, 2000, 122(1): 168-173.

[11] Biesuz M, Karacasulu L, Vakifahmetoglu C, et al. On the temperature measurement during ultrafast high-temperature sintering (UHS): Shall we trust metal-shielded thermocouples?[J]. Journal of the European Ceramic Society, 2024, 44(5): 3479-3485.

[12] Barzola-Quiquia J, Esquinazi P, Villafuerte M, et al. Origin of the giant negative photoresistance of ZnO single crystals[J]. Journal of Applied Physics, 2010, 108(7): 073530.

[13] Li Z, Liu F, Tang Y, et al. Compensated pyroelectric infrared detector based on Mn-doped PIMNT single crystal with enhanced signal stability[J]. Journal of The American Ceramic Society, 2020, 104(2): 995-1001.

[14] Mafi E, Calvano N, Patel J, et al. Electro-optical properties of sputtered calcium lead titanate thin films for pyroelectric detection[J]. Micromachines, 2020, 11(12): 1073.

[15] Hangauer A, Chen J, Strzoda R, et al. Performance of a fire detector based on a compact laser spectroscopic carbon monoxide sensor[J]. Optics Express, 2014, 22(11): 13680-13690.

[16] Zhang Z H, Zhang J W, Cao C F, et al. Temperature-responsive resistance sensitivity controlled by L-ascorbic acid and silane co-functionalization in flame-retardant GO network for efficient fire early-warning response [J]. Chemical Engineering Journal, 2020, 386123894.

[17] Liang M, Sun B J, Sun X G, et al. Development of a new fiber-optic multi-target multispectral pyrometer for achievable true temperature measurement of the solid rocket motor plume [J]. Measurement, 2017, 95239-245.

[18] Akula A, Ghosh R, Kumar S, et al. WignerMSER: Pseudo-wigner distribution enriched MSER feature detector for object recognition

in thermal infrared images[J]. Ieee Sensors Journal, 2019, 19(11): 4221-4228.

[19] Kruse P W. A comparison of the limits to the performance of thermal and photon detector imaging arrays[J]. Infrared Physics & Technology, 1995, 36(5): 869-882.

[20] Diamant G, Halahmi E, Kronik L, et al. Integrated circuits based on nanoscale vacuum phototubes[J]. Applied Physics Letters, 2008, 92(26): 262903.

[21] Daanoune M, Clerc R, Flament B, et al. Physics of trap assisted photomultiplication in vertical organic photoresistors[J]. Journal of Applied Physics, 2020, 127(5): 055502.

[22] Jia Y F, Liu P P, Bao L X, et al. Transduction of UV-light energy into alternating-current electricity via a neglected internal photoelectric effect of metal foil-based nanogenerator [J]. Nano Energy, 2024, 120.

[23] Lin C H, Liu C W. Metal-insulator-semiconductor photodetectors[J]. Sensors, 2010, 10(10): 8797-8826.

[24] Qiu Q, Huang Z. Photodetectors of 2D materials from utraviolet to terahertz waves[J]. Advanced Materials, 2021, 33(15): e2008126.

[25] Ouyang W, Teng F, He J H, et al. Enhancing the photoelectric performance of photodetectors based on metal oxide semiconductors by charge-carrier engineering[J]. Advanced Functional Materials, 2019, 29(9): 1807672.

[26] Liu W D, Yu Y, Dargusch M, et al. Carbon allotrope hybrids advance thermoelectric development and applications[J]. Renewable and Sustainable Energy Reviews, 2021, 141110800.

[27] Liu Y, Guo J, Zhu E, et al. Approaching the schottky-mott limit in van der Waals metal-semiconductor junctions[J]. Nature, 2018, 557(7707): 696-700.

[28] Shakeel M, Rehman K, Ahmad S, et al. A weldless approach for thermocouple fabrication through direct ink writing technique[J]. IEEE Sensors Journal, 2021, 21(2): 1279-1286.

[29] Zhou M, Zhao Y K, Zhang Q Y, et al. Enhance the responsivity of self-driven ultraviolet photodetector by (Al, Ga)N nanowire/graphene/PVDF heterojunction with high stability[J]. Optics Letters, 2024, 49(2): 338-341.

[30] Li S P, Lei T, Yan Z X, et al. High responsivity photodetectors based on graphene/WSe_2 heterostructure by photogating effect [J]. Chinese Physics B, 2024, 33(1).

[31] Li H Z, Shi Z Y, Que L C, et al. Modeling of graphene photodetector based on photogating effect for circuits simulation [J]. Physica Scripta, 2024, 99(1).

[32] Long M Q, Tang L, Wang D, et al. Theoretical predictions of size-dependent carrier mobility and polarity in graphene[J]. Journal of The American Chemical Society, 2009, 131(49): 17728-17729.

[33] Guo Y F, Zhang H T, Liu Y W, et al. Molecular-scale grinding of uniform small-size graphene flakes for use as lubricating oil additives[J]. New Carbon Materials, 2023, 38(5): 954-963.

[34] Wu Z L, Wang C W, Zhang X X, et al. Graphene-based CO_2 reduction electrocatalysts: A review[J]. New Carbon Materials, 2024, 39(1): 100-130.

[35] Kumar S, Goswami M, Singh N, et al. Flexible and lightweight graphene grown by rapid thermal processing chemical vapor deposition for thermal management in consumer electronics[J]. New Carbon Materials, 2023, 38(3): 534-540.

[36] Luo M Y, Xu R G, Shi Y, et al. Graphene with KI-modified pore structure and its electrochemical capacitors application[J]. New Carbon Materials, 2023, 38(2): 317-325.

[37] Zhang S S, Tu C J, Li X, et al. Sulfonated graphene improves the wear resistance of pantograph carbon slider materials under normal and wet conditions[J]. New Carbon Materials, 2023, 38(2): 378-383.

[38] Yao G, Ling F R, Yue J, et al. Dual-band tunable perfect metamaterial absorber in the THz range[J]. Optics Express, 2016, 24(2): 1518-1527.

[39] Nair R R, Blake P, Grigorenko A N, et al. Fine structure constant defines visual transparency of graphene[J]. Science, 2008, 320(5881): 1308-1308.

[40] Li X M, Zhu M, Du M D, et al. High detectivity graphene-silicon heterojunction photodetector[J]. Small, 2016, 12(5): 595-601.

[41] Ahmadi E, Asgari A. Modeling of the infrared photodetector based on multi layer armchair graphene nanoribbons[J]. Journal of Applied Physics, 2013, 113(9): 093106.

[42] Nalwa H S. A review of molybdenum disulfide (MoS_2) based photodetectors: from ultra-broadband, self-powered to flexible devices[J]. RSC Advances, 2020, 10(51): 30529-30602.

[43] Singh E, Singh P, Kim K S, et al. Flexible molybdenum disulfide (MoS_2) atomic layers for wearable electronics and optoelectronics[J]. ACS Applied Materials & Interfaces, 2019, 11(12): 11061-11105.

[44] Singh E, Kim K S, Yeom G Y, et al. Atomically thin-layered molybdenum disulfide (MoS_2) for bulk-heterojunction solar cells[J]. ACS Applied Materials & Interfaces, 2017, 9(4): 3223-3245.

[45] Kang B, Kim Y, Yoo W J, et al. Ultrahigh photoresponsive device based on ReS_2/graphene heterostructure[J]. Small, 2018, 14(45): e1802593.

[46] Zhao Y, Tsai T Y, Wu G, et al. Graphene/SnS_2 van der Waals photodetector with high photoresponsivity and high photodetectivity for broadband 365-2240 nm detection[J]. ACS Applied Materials Interfaces, 2021, 13(39): 47198-47207.

[47] Long M, Liu F, Ding F, et al. Scalable fabrication of long-wave infrared $PtSe_2$-G heterostructure array photodetectors[J]. Applied Physics Letters, 2020, 117(23): 231104.

[48] Wu D, Zhao Z, Lu W, et al. Highly sensitive solar-blind deep ultraviolet photodetector based on graphene/$PtSe_2$/β-Ga_2O_3 2D/3D Schottky junction with ultrafast speed[J]. Nano Research, 2021, 14(6): 1973-1979.

[49] Ren Y, Dai T, He B, et al. Fabrication of high-gain photodetector with graphene-PbSe heterostructure[J]. IEEE Electron Device Letters, 2019, 40(1): 48-50.

[50] Manga K K, Wang J, Lin M, et al. High-performance broadband photodetector using solution-processible PbSe-TiO_2-graphene hybrids[J]. Advanced Materials, 2012, 24(13): 1697-702.

[51] Lu R, Liu J, Luo H, et al. Graphene/GaSe-nanosheet hybrid:

Towards high gain and fast photoresponse [J]. Scientific Reports, 2016, 619161.

[52] Mudd G W, Svatek S A, Hague L, et al. High broad-band photoresponsivity of mechanically formed InSe-graphene van der Waals heterostructures[J]. Advanced Materials, 2015, 27(25): 3760-6.

[53] Gao W, Zheng Z, Li Y, et al. High performance tin diselenide photodetectors dependent on thickness: A vertical graphene sandwiched device and interfacial mechanism[J]. Nanoscale, 2019, 11(28): 13309-13317.

[54] Yan F, Zhao L, Patane A, et al. Fast, multicolor photodetection with graphene-contacted p-GaSe/n-InSe van der Waals heterostructures[J]. Nanotechnology, 2017, 28(27): 27LT01.

[55] Gao A, Liu E, Long M, et al. Gate-tunable rectification inversion and photovoltaic detection in graphene/WSe_2 heterostructures[J]. Applied Physics Letters, 2016, 108(22): 223501.

[56] Islam S, Mishra J K, Kumar A, et al. Ultra-sensitive graphene-bismuth telluride nano-wire hybrids for infrared detection[J]. Nanoscale, 2019, 11(4): 1579-1586.

[57] Noumbe U N, Greboval C, Livache C, et al. Reconfigurable 2D/0D p-n graphene/HgTe nanocrystal heterostructure for infrared detection[J]. ACS Nano, 2020, 14(4): 4567-4576.

[58] Iqbal M Z, Khan S, Siddique S. Ultraviolet-light-driven photoresponse of chemical vapor deposition grown molybdenum disulfide/graphene heterostructured FET [J]. Applied Surface Science, 2018, 459853-859.

[59] Lee I, Kang W T, Kim J E, et al. Photoinduced tuning of schottky barrier height in graphene/MoS_2 heterojunction for ultrahigh performance short channel phototransistor[J]. ACS Nano, 2020, 14(6): 7574-7580.

[60] Rathi S, Lee I, Lim D, et al. Tunable electrical and optical characteristics in monolayer graphene and few-layer MoS_2 heterostructure devices[J]. Nano Letters, 2015, 15(8): 5017-24.

[61] Yu W J, Liu Y, Zhou H, et al. Highly efficient gate-tunable photocurrent generation in vertical heterostructures of layered materials[J]. Nature Nanotechnology, 2013, 8(12): 952-8.

[62] Xiao P, Mao J, Ding K, et al. Solution-processed 3D RGO-MoS_2/pyramid Si heterojunction for ultrahigh detectivity and ultra-broadband photodetection[J]. Advanced Materials, 2018, 30(31): e1801729.

[63] Xu H, Han X, Dai X, et al. High detectivity and transparent few-layer MoS_2/glassy-graphene heterostructure photodetectors[J]. Advanced Materials, 2018, 30(13): e1706561.

[64] Gao S, Wang Z Q, Wang H D, et al. Graphene/MoS_2/graphene vertical heterostructure-based broadband photodetector with high performance[J]. Advanced Materials Interfaces, 2021, 8(3): 2001730.

[65] Li H, Li X, Park JH, et al. Restoring the photovoltaic effect in graphene-based van der Waals heterojunctions towards self-powered high-detectivity photodetectors [J]. Nano Energy, 2019, 57214-221.

[66] Vu Q A, Lee J H, Nguyen V L, et al. Tuning carrier tunneling in van der Waals heterostructures for ultrahigh detectivity[J]. Nano Letters, 2017, 17(1): 453-459.

[67] Chen Z, Zhang Z, Biscaras J, et al. A high performance self-driven photodetector based on a graphene/InSe/MoS_2 vertical heterostructure[J]. Journal of Materials Chemistry C, 2018, 6(45): 12407-12412.

[68] Long M, Liu E, Wang P, et al. Broadband photovoltaic detectors based on an atomically thin heterostructure[J]. Nano Letters, 2016, 16(4): 2254-2259.

[69] Wallace P R. The band theory of graphite[J]. Physical Review X, 1947, 71(9): 622-634.

[70] Wang F, Yin L, Wang Z, et al. Strong electrically tunable $MoTe_2$/graphene van der Waals heterostructures for high-performance electronic and optoelectronic devices[J]. Applied Physics Letters, 2016, 109(19): 193111.

[71] Li A, Chen Q, Wang P, et al. Ultrahigh-sensitive broadband photodetectors based on dielectric shielded $MoTe_2$/graphene/SnS_2 p-g-n junctions[J]. Advanced Materials, 2019, 31(6): e1805656.

[72] Mak K F, Lee C, Hone J, et al. Atomically thin MoS_2: A new direct-gap semiconductor[J]. Physical Review Letters, 2010, 105(13): 136805.

[73] Lin H, Sturmberg B C P, Lin K T, et al. A 90-nm-thick graphene metamaterial for strong and extremely broadband absorption of unpolarized light[J]. Nature Photonics, 2019, 13(4): 270.

[74] Vabbina P, Choudhary N, Chowdhury A A, et al. Highly sensitive wide bandwidth photodetector based on internal photoemission in CVD grown p-type MoS_2/graphene schottky junction[J]. ACS Applied Materials Interfaces, 2015, 7(28): 15206-15213.

[75] Liu B Y, You C Y, Zhao C, et al. High responsivity and near-infrared photodetector based on graphene/$MoSe_2$ heterostructure[J]. Chinese Optics Letters, 2019, 17(2): 020002.

[76] De Fazio D, Goykhman I, Yoon D, et al. High responsivity, large-area graphene/MoS_2 flexible photodetectors[J]. ACS Nano, 2016, 10(9): 8252-8262.

[77] Roy K, Padmanabhan M, Goswami S, et al. Graphene-MoS_2 hybrid structures for multifunctional photoresponsive memory devices[J]. Nature Nanotechnology, 2013, 8(11): 826-830.

[78] Xu H, Wu J X, Feng Q L, et al. High responsivity and gate tunable graphene-MoS_2 hybrid phototransistor[J]. Small, 2014, 10(11): 2300-2306.

[79] Zhang W, Chuu C P, Huang J K, et al. Ultrahigh-gain photodetectors based on atomically thin graphene-MoS_2 heterostructures [J]. Scientific Reports, 2014, 43826.

[80] Massicotte M, Schmidt P, Vialla F, et al. Photo-thermionic effect in vertical graphene heterostructures [J]. Nature Communications, 2016, 712174.

[81] Wang Q, Yesilyurt C, Liu F, et al. Anomalous photothermoelectric transport due to anisotropic energy dispersion in WTe_2[J]. Nano Letters, 2019, 19(4): 2647-2652.

[82] Zhang Y, Li H, Wang L, et al. Photothermoelectric and photovoltaic effects both present in MoS_2 [J]. Scientific Reports, 2015, 57938.

[83] Cai X, Sushkov A B, Suess R J, et al. Sensitive room-temperature terahertz detection via the photothermoelectric effect in

graphene[J]. Nature Nanotechnology, 2014, 9(10): 814-819.

[84] Li X B, Wu J X, Mao N N, et al. A self-powered graphene-MoS_2 hybrid phototransistor with fast response rate and high on-off ratio [J]. Carbon, 2015, 92126-92132.

[85] Oh G, Jeon J H, Kim Y C, et al. Gate-tunable photodetector and ambipolar transistor implemented using a graphene/$MoSe_2$ barristor [J]. NPG Asia Materials, 2021, 13 (1): 13: 10.

[86] Li X, Wu J, Mao N, et al. A self-powered graphene–MoS_2 hybrid phototransistor with fast response rate and high on–off ratio [J]. Carbon, 2015, 92126-92132.

[87] Liu B, Zhao C, Chen X, et al. Self-powered and fast photodetector based on graphene/$MoSe_2$/Au heterojunction [J]. Superlattices and Microstructures, 2019, 13087-13092.

[88] Giovannetti G, Khomyakov P A, Brocks G, et al. Doping graphene with metal contacts[J]. Physical Review Letters, 2008, 101(2): 026803.

[89] Li X, Zhao T, Chen Q, et al. Flexible all solid-state supercapacitors based on chemical vapor deposition derived graphene fibers[J]. Physical Chemistry Chemical Physics, 2013, 15(41): 17752-17757.

[90] Baik S S, Im S, Choi H J. Work function tuning in two-dimensional MoS_2 field-effect-transistors with graphene and titanium source-drain contacts [J]. Scientific Reports, 2017, 745546.

[91] Hibino H, Kageshima H, Kotsugi M, et al. Dependence of electronic properties of epitaxial few-layer graphene on the number of layers investigated by photoelectron emission microscopy[J]. Physical Review B, 2009, 79(12): 125437.

[92] Jeong H K, Kim K-j, Kim S M, et al. Modification of the electronic structures of graphene by viologen[J]. Chemical Physics Letters, 2010, 498(1-3): 168-171.

[93] Shi Y M, Kim K K, Reina A, et al. Work function engineering of graphene electrode via chemical doping[J]. ACS Nano, 2010, 4(5): 2689-2694.

[94] Long M S, Wang P, Fang H H, et al. Progress, challenges, and opportunities for 2D material based photodetectors[J]. Advanced Functional Materials, 2019, 29(19): 1803807.

[95] Dong H, Chen K, Yang H, et al. Innovative all-silicon based a-SiNx: O/c-Si heterostructure solar-blind photodetector with both high responsivity and fast response speed[J]. APL Photonics, 2022, 7(2): 026102.

[96] Ni Z Y, Ma L L, Du S C, et al. Plasmonic silicon quantum dots enabled high-sensitivity ultrabroadband photodetection of graphene-based hybrid phototransistors[J]. ACS Nano, 2017, 11(10): 9854-9862.

[97] Guan X, Yu X, Periyanagounder D, et al. Recent progress in short to long wave infrared photodetection using 2D materials and heterostructures[J]. Advanced Optical Materials, 2020, 9(4): 2001708.

[98] Ma Y, Qu H, Wang W, et al. Si/SiO_2@graphene superstructures for high performance lithium-ion batteries[J]. Advanced Functional Materials, 2022, 33(8): 2211648.

[99] Frisenda R, Molina-Mendoza A J, Mueller T, et al. Atomically thin p-n junctions based on two-dimensional materials[J]. Chemical Society Reviews, 2018, 47(9): 3339-3358.

[100] Yang Z, Zhou Y, Ramanathan S. Studies on room-temperature electric-field effect in ionic-liquid gated VO_2 three-terminal devices [J]. Journal of Applied Physics, 2012, 111 (1).

[101] Liu F, Ming P, Li J. Ab initio calculation of ideal strength and phonon instability of graphene under tension[J]. Physical Review, 2007, 76(6): 064120.1-064120.7.

[102] Voiry D, Mohite A, Chhowalla M. Phase engineering of transition metal dichalcogenides[J]. Chemical Society Reviews, 2015, 44(9): 2702-2712.

[103] Wang W Z, Zeng X B, Warner J H, et al. Photoresponse-bias modulation of a high-performance MoS_2 photodetector with a unique vertically stacked 2H-MoS_2/1T@2H-MoS_2 structure[J]. ACS Applied Materials Interfaces, 2020, 12(29): 33325-33335.

[104] Kwak J Y. Absorption coefficient estimation of thin MoS_2 film using attenuation of silicon substrate Raman signal [J]. Results Phys, 2019, 13102202.

[105] Hu W, Wang T, Zhang R, et al. Effects of interlayer coupling and electric fields on the electronic structures of graphene and MoS_2 heterobilayers[J]. Journal of Materials Chemistry C, 2016, 4(9): 1776-1781.

[106] Zan W Y, Geng W, Liu H X, et al. Influence of interface structures on the properties of molybdenum disulfide/graphene composites: A density functional theory study [J]. Journal of Alloys and Compounds, 2015, 649961-967.

[107] Robledo A R, Salazar M F, Martínez B A M, et al. Interlayer charge transfer in supported and suspended MoS_2/graphene/MoS_2 vertical heterostructures[J]. Plos One, 2023, 18(7): e0283834.

[108] Gupta S, Johnston A, Khondaker S. Optoelectronic properties of MoS_2/graphene heterostructures prepared by dry transfer for light-induced energy applications[J]. Journal of Electronic Materials, 2022, 51(8): 4257-4269.

[109] Finn D J, Lotya M, Cunningham G, et al. Inkjet deposition of liquid-exfoliated graphene and MoS_2 nanosheets for printed device applications[J]. Journal of Materials Chemistry C, 2014, 2(5): 925-932.

[110] Liu L X, Zhai T Y. Wafer-scale vertical van der Waals heterostructures[J]. Infomat, 2021, 3(1): 3-21.

[111] Chen T, Zhou Y, Sheng Y, et al. Hydrogen-assisted growth of large-area continuous films of MoS_2 on monolayer graphene[J]. ACS Applied Materials Interfaces, 2018, 10(8): 7304-7314.

[112] Dean C R, Young A F, Meric I, et al. Boron nitride substrates for high-quality graphene electronics[J]. Nature Nanotechnology, 2010, 5(10): 722-726.

[113] Li H, Wu J M T, Huang X, et al. A universal, rapid method for clean transfer of nanostructures onto various substrates[J]. ACS Nano, 2014, 8(7): 6563-6570.

[114] Wang P J, Song S P, Najafi A, et al. High-fidelity transfer of chemical vapor deposition grown 2D transition metal dichalcogenides via substrate decoupling and polymer/small molecule composite[J]. ACS Nano, 2020, 14(6): 7370-7379.

[115] Kwon K C, Choi S, Hong K, et al. Wafer-scale transferable

molybdenum disulfide thin-film catalysts for photoelectrochemical hydrogen production[J]. Energy & Environmental Science, 2016, 9(7): 2240-2248.

[116] Liu Y, Zhang S, He J, et al. Recent progress in the fabrication, properties, and devices of heterostructures based on 2D materials[J]. Nano-Micro Letters, 2019, 11(1): 13.

[117] Cao X H, Shi Y M, Shi W H, et al. Preparation of MoS_2-coated three-dimensional graphene networks for high-performance anode material in lithium-ion batteries[J]. Small, 2013, 9(20): 3433-3438.

[118] Tang Y, Cong H, Chen Z, et al. An array of Eiffel-tower-shape AlN nanotips and its field emission properties [J]. Applied Physics Letters, 2005, 86 (23).

[119] Lan C Y, Dong R T, Zhou Z Y, et al. Large-scale synthesis of freestanding layer-structured PbI_2 and $MAPbI_3$ nanosheets for high-performance photodetection[J]. Advanced Materials, 2017, 29(39): 1702759.

[120] Yu F F, Liu Q W, Gan X, et al. Ultrasensitive pressure detection of few-layer MoS_2[J]. Advanced Materials, 2017, 29(4): 1603266.

[121] Tao J G, Chai J W, Lu X, et al. Growth of wafer-scale MoS_2 monolayer by magnetron sputtering[J]. Nanoscale, 2015, 7(6): 2497-2503.

[122] Flory N, Ma P, Salamin Y, et al. Waveguide-integrated van der Waals heterostructure photodetector at telecom wavelengths with high speed and high responsivity[J]. Nature Nanotechnology, 2020, 15(2): 118-124.

[123] Zhang K, Fang X, Wang Y, et al. Ultrasensitive near-infrared photodetectors based on a graphene-$MoTe_2$-graphene vertical van der Waals heterostructure[J]. ACS Applied Materials Interfaces, 2017, 9(6): 5392-5398.

[124] Xiong Y F, Chen J H, Lu Y Q, et al. Broadband optical-fiber-compatible photodetector based on a graphene-MoS_2-WS_2 heterostructure with a synergetic photogenerating mechanism[J]. Advanced Electronic Materials, 2019, 5(1): 1800562.

[125] Liu Q, Cook B, Gong M, et al. Printable transfer-free and wafer-size MoS_2/graphene van der Waals heterostructures for high-performance photodetection[J]. ACS Applied Materials Interfaces, 2017, 9(14): 12728-12733.

[126] Liu K H, Zhang L M, Cao T, et al. Evolution of interlayer coupling in twisted molybdenum disulfide bilayers [J]. Nature Communications, 2014, 54966.

[127] Jang A R. Tuning schottky barrier of single-layer MoS_2 field-effect transistors with graphene electrodes[J]. Nanomaterials, 2022, 12(17): 3038.

[128] Li P K, Guo H T, Duan R, et al. Excellent optoelectronic properties and low contact resistance of graphene/MoS_2 heterostructure optoelectronic devices: First- principles calculation and experimental verification[J]. ACS Applied Electronic Materials, 2023, 5(3): 1676-1687.

石墨烯/钼基二硫族化合物范德华异质结光电探测器的研究进展

张鑫华[1,†]，　刘伟迪[2,†]，　龚佑品[3,*]，　刘庆丰[1,*]，　陈志刚[2,*]

（1. 南京工业大学 化工学院，材料化学工程国家重点实验室，江苏 南京 211816；
2. School of Chemistry and Physics, ARC Research Hub in Zero-emission Power Generation for Carbon Neutrality, and Center for Materials Science, Queensland University of Technology, Brisbane, QLD 4000, Australia；
3. 重庆大学 物理学院，前沿交叉学科研究院量子材料与器件研究中心，重庆 400044）

摘　要： 石墨烯因其高载流子迁移率和宽光谱吸收范围而广泛应用于光电探测。然而，其低光吸收率导致的高暗电流严重限制了它的光电探测性能。钼基二硫族化合物（MoX_2，X = S、Se 和 Te）具有高的吸收系数，能够弥补石墨烯基光电探测器中暗电流较高的劣势，因此基于石墨烯/MoX_2 范德华异质结的光电探测器能够表现出优异的光电子特性。本综述首先回顾了光电探测器的工作原理、性能指标和结构。之后，从材料基础的角度突出了石墨烯/MoX_2 范德华异质结光电探测器的重要性。接着，总结了石墨烯/MoX_2 范德华异质结光电探测器的制备方法和性能增强策略。最后，强调了这类异质结光电探测器当前面临的挑战及未来的发展方向。本综述将为这类高性能范德华异质结光电探测器的设计提供一定的指导和参考。

关键词： 石墨烯；钼基二硫族化合物；异质结；光电探测器；范德华

中图分类号： 127.1$^+$1　　**文献标识码：** A

通讯作者： 龚佑品，副教授. E-mail: gongyp@cqu.edu.cn；
刘庆丰，教授. E-mail: qfliu@njtech.edu.cn；
陈志刚，教授. E-mail: zhigang.chen@qut.edu.au

作者简介：[†]张鑫华和刘伟迪为共同第一作者

本文的电子版全文由 Elsevier 出版社在 ScienceDirect 上出版（https://www.sciencedirect.com/journal/new-carbon-materials/）